

This is the peer reviewed version of the following article: Bhatt A., et al. ChemBioChem 2017, 18, 213 – 222, which has been published in final form at <https://chemistry-europe.onlinelibrary.wiley.com/doi/full/10.1002/cbic.201600513>. This article may be used for non-commercial purposes in accordance with Wiley Terms and Conditions for Use of Self-Archived Versions

Structure activity relationships of benzenesulfonamide-based inhibitors towards carbonic anhydrase isoform specificity

Avni Bhatt^a, Brian P. Mahon^a, Vinicius Wilian D. Cruzeiro^{b,c}, Benedetta Cornelio^{d,e}, Marie Laronze-Cochard^d, Mariangela Ceruso^f, Janos Sapi^d, Graham A. Rance^g, Andrei N. Khlobystov^g, Antonella Fontana^c, Adrian Roitberg^b, Claudiu T. Supuran^f, Robert McKenna^{a,†}

^a Department of Biochemistry and Molecular Biology, College of Medicine, University of Florida, PO Box 100245, Gainesville FL 32610, USA

^b Department of Chemistry, College of Liberal Arts and Sciences, University of Florida, PO Box 117200, Gainesville FL 32610, USA

^c CAPES Foundation, Ministry of Education of Brazil, Brasília – DF 70040-020, Brazil

^d Institut de Chimie Moléculaire de Reims, CNRS UMR 7312, Université de Reims Champagne-Ardenne, UFR Pharmacie, 51 Rue Cognacq-Jay, F-51096 Reims Cedex, France

^e Dipartimento di Farmacia, Università "G. d'Annunzio", Via dei Vestini, I-66100 Chieti, Italy

^f Laboratorio de Chimica Bioinorganica, Rm. 188, Università degli Studi di Firenze, Via della Lastruccia 3, 50019 Sesto Fiorentino, Florence, Italy

^g School of Chemistry, The University of Nottingham, University Park, Nottingham, NG7 2RD, UK

[†] Corresponding Author:

Tel: +1 (352) 392-5696, Fax: +1 (352) 392-3422, Email: rmckenna@ufl.edu

Key words: carbonic anhydrase, benzenesulfonamide, selective inhibition, structure-activity relationships, X-ray crystallography,

Abstract

Carbonic anhydrases (CAs) are implicated in a wide range of diseases, including the upregulation of isoforms CA IX and XII in many aggressive cancers. However, effective inhibition of disease-implicated CAs should minimally affect the ubiquitously expressed isoforms, including CA I and II, to improve directed distribution of the inhibitors to the cancer-associated isoforms and reduce side effects. Four benzenesulfonamide-based inhibitors were synthesized by using the tail approach and displayed nanomolar affinities for several CA isoforms. The crystal structures of the inhibitors bound to a CA IX mimic and CA II are presented. Further *in silico* modeling was performed with the inhibitors docked into CA I and XII to identify residues that contributed to or hindered their binding interactions. These structural studies demonstrated that active-site residues lining the hydrophobic pocket, especially positions 92 and 131, dictate the positional binding and affinity of inhibitors, whereas the tail groups modulate CA isoform specificity. Geometry optimizations were performed on each ligand in the crystal structures and showed that the energetic penalties of the inhibitor conformations were negligible compared to the gains from active-site interactions. These studies further our understanding of obtaining isoform specificity when designing small molecule CA inhibitors.

Introduction

Carbonic anhydrases (CAs) are zinc metalloenzymes that catalyze the interconversion of carbon dioxide to bicarbonate. Humans express 16 CA isoforms, of which 13 are catalytically active and have been shown to be involved in multiple physiological processes such as respiration, pH regulation, bone resorption, and formation of the gastric environment. CA isoforms have specific subcellular localization, with examples that include the mitochondrial CA Va and Vb, cytosolic CA I and II, and extracellular membrane-bound CA IX and XII.[1] Many human CA isoforms are also established drug targets for a variety of diseases, including diabetes, glaucoma, epilepsy, and more recently, cancer.[2]

In several types of cancer, CA IX and XII are upregulated and have been shown to be useful prognostic markers. Ongoing studies are establishing the roles of these isoforms in regulating the tumor microenvironment and, as such, they are both being studied as drug targets. CA IX is normally localized to the gut epithelium but is highly upregulated in hypoxic tumors exhibiting acidic extracellular environments.[3] The acidic tumor microenvironment is caused by a metabolic shift to the anaerobic glycolytic pathway to facilitate rapid cell proliferation in the absence of surrounding vasculature, a process known as the Warburg effect that results in the production and export of lactic acid.[4–8] CA IX upregulation and activity has been shown to be important for tumor viability, and its inhibition results in a favorable therapeutic response in hypoxic and aggressive tumors.[3, 6, 9] Recent studies have also suggested the importance of CA XII upregulation, both in conjunction with CA IX or in CA IX-deficient tumors. However, the role of CA XII in maintaining the tumor microenvironment is still being studied, although it is known to also be expressed in several normal tissue types such as kidney, pancreas, breast, and prostate.[10, 11] In the case of triple-negative breast cancer (ER-, PR-, HER2-), upregulation of both CA IX

and XII is correlated with poor patient prognosis.[11–14]

CA IX and XII share sequence identity and structural homology with other ubiquitously expressed isoforms (34% sequence identity with the ubiquitously expressed CA II), making the design of isoform-specific inhibitors challenging. As CA I and II are expressed in red blood cells, binding to these isoforms during drug administration would lessen the efficacy of CA inhibitors targeting tumor sites and would result in undesired inhibition of these essential CA isoforms for blood pH regulation.

Most human CA active sites are divided into two distinct sides: a hydrophilic and a hydrophobic side. The catalytic zinc atom is centered at the base of the active-site cleft and is tetrahedrally coordinated by three histidine residues (His94/96/119) and a solvent molecule. Most human CA isoforms have additional conserved His64 (a lysine in CA III) and Tyr7 residues critical for catalytic function (CA II numbering).[15, 16] The catalytic mechanism is a two-step process. In the hydration reaction, the first step is the nucleophilic attack of CO₂ by the zinc-coordinated hydroxide to form bicarbonate, which is subsequently displaced by a water molecule and released.[2] The second step of the reaction is the regeneration of the zinc-coordinated hydroxide by a proton transfer mechanism through a series of well-ordered solvent molecules and His64, which resides on the edge of the active-site cavity.[17–19]

All current clinically used CA inhibitors contain a sulfonamide or a structurally related sulfamido or sulfamato group that functions as the zinc binding group (ZBG) to resemble a transition state analogue similar to the tetrahedrally coordinated zinc to bicarbonate.[20–22] Although this mode of binding inhibits catalysis, it alone shows minimal CA isoform specificity due to the conservation of residues deep within the active site. The residues that distinguish the isoforms are located away from the zinc and are primarily residues towards the active-site entrance (Table 1).[23–25] Some

of these residue differences modulate hydrophobicity and charge; others change the active-site cavity volume and shape. These differences in active-site environment in turn modulate inhibitor binding constants and their dynamics of entry.[26]

This study investigates the binding of four benzenesulfonamide-based inhibitors with the cancer-associated targets, CA IX and XII, and the off-target CA I and II. The ligands were synthesized by using the tail approach,[27] in that they share the same **ZBG** and benzene linker region, but differ in their tail group to permit functional diversity.[20, 22–24, 28] The crystal structures of the inhibitors were determined with CA II and an engineered CA IX mimic, and molecular docking was performed with CA IX and CA I. Furthermore, the conformational energy of each ligand in the crystal structures were calculated to understand the favorability of adopting their observed conformations.

These values are discussed in relation to the measured K_i values of the inhibitors bound to the CA isoforms. The high affinity (nM) for isoforms II, IX, and XII, and their small size (MW=250–290 Da) make them attractive lead compounds for the design of more isoform selective inhibitors.

Results and Discussion

Inhibitor design and synthesis

The syntheses of the inhibitors, referred to as compounds **4a**, **4b**, **4e**, and **4p**, were published previously by Cornelio et al.[29] as part of a larger series of benzenesulfonamide-based inhibitors with aryl substitutions in the para position of the benzene ring (Table 2). In brief, syntheses were performed in two-step reactions comprising a crucial Suzuki–Miyaura cross-coupling, mediated by an original nanocatalyst. All compounds contained a sulfonamide **ZBG** and a benzene linker ring with various tail ring moieties.[24, 27] The tail variants stem from the scaffold molecule, 4-

(phenyl)benzenesulfonamide (**4a**), molecular weight: 233.29 gmol⁻¹. The variants were: **4b**, 4-(2'-methylphenyl)

benzenesulfonamide containing a hydrophobic methyl substituent at position C2', molecular weight: 247.31 gmol⁻¹; **4e**, 4-(3'-formylphenyl)benzenesulfonamide, containing a formyl group at position C3', molecular weight: 261.3 gmol⁻¹; and **4p**, 4-(3'-quinolinyl)benzenesulfonamide, a heterocyclic fused quinoline ring, molecular weight: 284.30 gmol⁻¹ (carbon atom numbering is given in Table 2).

CA inhibition profile

For the cytosolic CA I, compounds **4b** and **4e** displayed only weak affinity (mm range), with K_i values of 3500 and 1200 nM, respectively; compounds **4a** and **4p** had relatively stronger affinity, with K_i values of 42 and 35 nM, respectively. In contrast, all four compounds bound with high affinity (0.8–2.5 nM) to CA II (Table 2).

For the extracellular cancer-related CAs, a different binding affinity pattern was observed. Compounds **4a** and **4p** exhibited sub-nanomolar affinity of 0.2 nM to CA IX; **4b** and **4e** bound with lower affinity, with K_i values of 20 and 99 nM, respectively. The binding profiles for CA XII were mixed, from weak affinity for compound **4p** (760 nM) to sub-nanomolar affinity (0.6 nM) for compound **4e** (Table 2). As such, this variation in inhibition constants for the four compounds resulted in a large range of CA-selective inhibition.

We next considered CA IX inhibition over the cytosolic ubiquitously expressed CA I and II. Compound **4a** had 200-fold selectivity for CA IX over CA I, but only fourfold selectivity over CA II. Similarly, compound **4b** had 200-fold selectivity for CA IX over CA I but again had moderate 16-fold selectivity over CA II. Compound **4e** had a modest tenfold selectivity for CA IX over CA

I, but showed preferential affinity for CA II. Compound **4p** exhibited 180-fold selectivity for CA IX over CA I and again, a modest tenfold selectivity over CA II (Table 3).

Finally, the selectivity for CA XII over CA II and I was considered. Compound **4e** showed the highest selectivity over CA I, with 2000-fold selectivity, but had a modest threefold selectivity over CA II. Compounds **4a**, **4b**, and **4p** were all poor candidates for CA XII targeting, with **4a** and **4p** showing two- and 20-fold selectivity for CA II over CA XII, respectively. The selectivities of the compounds were also compared to inhibition constants for acetazolamide (**AZM**), a clinically used CA inhibitor that is considered non-isoform-specific and had K_i values ranging from 5.7 to 250 nM (Table 2).

X-ray crystallography data and analysis

Crystal structures of CA II and the CA IX mimic were all determined in complex with compounds **4a**, **4b**, **4e**, and **4p** in order to determine specific interactions that might have contributed to the K_i value and observed CA isoform specificity. All eight structures were solved to high resolutions between 1.15 and 1.78 Å (Table 4), with clear electron density observed for the bound inhibitors (Figure 1). The structures clearly showed that the inhibitors interacted with the active-site zinc atom through deprotonation of nitrogen on the sulfonamide group, as known from previous studies with sulfonamide-based inhibitors.[22, 28, 30] The linker benzene rings were oriented to span across the wide axis of the active sites, whereas the 4-aryl tail substituents adopted a variety of conformations, depending on the interactions, and with steric hindrance with residues in the respective active sites. The linker benzene ring also exhibited less conformational flexibility than the tail substituent, as indicated by electron contouring levels (Figure 1). All four inhibitors preferentially bound to the hydrophobic side of the active sites in both CA II and the CA IX mimic

(Figure 2).

Compound **4a** bound in an almost identical conformation in both the CA II and CA IX mimic structures, with the 4-phenyl ring making van der Waals (vdW) contacts with three residues (Pro202, Val135, Phe131) along the hydrophobic side of CA II and four residues (Pro202, Leu141, Val135, Val131) with the CA IX mimic. The 4a rings had dihedral angles of 31.7 and 66.48 (C3-C4-C1'-C2', see Table 2) for the CA IX mimic and CA II, respectively. Hence, the 4-phenyl ring was more twisted with respect to the linker ring in CA II. This is most likely due to the steric hindrance/interference caused by the presence of Phe131. The less twisted conformation of **4a** in the CA IX mimic permitted additional vdW interactions with Leu141 (Figure 2A and B).

The 4-(2-methylphenyl) tail of inhibitor **4b** established vdW interactions with four residues on the hydrophobic side of the CA II active site: Pro202, Leu198, Val135, and Phe131, while making seven interactions on the hydrophobic side of the CA IX mimic active site: Pro202, Leu198, Leu141, Val135, Val131, Val121, and Leu91 (Figure 2C and D). The 2-methyl substituent faced towards the hydrophobic pocket of the CA IX mimic, with a dihedral angle of 41.98 between the linker and 4-aryl tail ring. In contrast, the 2-methyl group faced away from the hydrophobic side of the CA II active site with a dihedral angle of 231.8, essentially exhibiting a 180° flip. This change in conformation is explained by steric hindrance of Phe131, which prevented the 2-methyl group from making contacts with residues along the pocket. Because of the smaller Val131 in the CA IX mimic, the 4-(2-methylphenyl) group of **4b** was able to place itself more tightly into the CA IX mimic hydrophobic pocket, resulting in more vdW contacts, including a weak interaction with Leu91, which could not occur for **4b** and Ile91 in CA II. Although more vdW interactions were present between **4b** and the CA IX mimic, these contacts were insufficient to increase the affinity of the compound for CA IX over CA II. This is likely due to the smaller active site of CA

II, which limits movement of the compound in and out of the active site more than is possible in the CA IX.

In the CA II complex with **4e**, two molecules were bound, one in the active site and the other between a crystal contact (Figure S1 in the Supporting Information). For the **4e** molecule bound in the active site, the 4-(3-formylphenyl) tail made vdW interactions with Pro202, Leu198, Val135, and Phe131, and the formyl group formed a weak hydrogen bond with Gln92 (3.2 a). In the CA IX mimic, the **4e** tail also makes vdW interactions with Pro202, Leu198, Leu141, Val135, Val131, and Val121, but the formyl group was not within distance to form any hydrogen bonds (Figure 2E and F). **4e** adopted a relatively planar conformation in CA IX mimic, with a dihedral angle along C3-C4-C1'-C2' of 200.8°. This conformation maximizes the number of hydrophobic contacts within the active site. In contrast, the dihedral angle of **4e** in CA II was 312°, again likely due to both the steric hindrance of Phe131 and the formation of the hydrogen bond between the formyl moiety and Gln92. It is also possible that the conformation of the tail ring also permits the formation of weak π -stacking interaction. Displacement of solvent molecules (red spheres in Figure 2) in the CA II active site could explain the approximately 50-fold higher affinity of **4e** for CA II over CA IX. However, it is important to note that a glycerol molecule was also bound within the active site of CA II along the hydrophilic side; this might have contributed to the solvent displacement (Figure S1). Overall, these two structures indicate that the 3-formyl group is primarily useful for preventing interactions with the hydrophobic pocket of the CA active site, and was highly unfavorable for creating isoform specific interactions with the CA IX mimic, most likely due to the lack of hydrogen bond formation. However, this group might be a useful substituent for creating a specific CA II inhibitor because this H-bond is observed (Figure 2E).

The **4e** molecule bound on the surface of CA II is located in a crystal contact pocket. The

sulfonamide is buried in a pocket within 2.7 Å of Asp19. Surrounding the pocket are several hydrophobic residues (Trp5, Trp16, Phe20), which provide a favorable binding environment for the hydrophobic benzene linker ring and 4-aryl tail. However, although the interactions of **4e** along this lattice interface are intriguing, they are most likely due to a crystallographic artifact through the packing of symmetry-related molecules.

The 4-(3-quinolinyl) tail of **4p** in complex with CA II established vdW interactions with Pro202, Leu198, Leu141, Val135, and Phe131. In the CA IX mimic, the **4p** tail made hydrophobic interactions with Pro202, Leu198, Leu141, Val135, Val131, and Leu91 (Figure 2G, H). Compound **4p** adopted a conformation in the CA IX mimic similar to that of **4a**, with a dihedral angle C3-C4-C1'-C2' of 36.2°. This orientation allowed for the maximum number of interactions along the hydrophobic pocket of the active site, including that with Leu91. The dihedral angle of **4p** in CA II was 71.7°, adopting a slightly more twisted conformation, again, because of the bulky Phe131 in the active site.

Ligand free energy calculations

Energy calculations were performed to quantify the energetic penalty of each ligand adopting the observed conformations in their respective crystal structures. The ΔE values (kcalmol^{-1}) calculated from the difference between the energy of the most favorable conformation of each ligand in a stable water dielectric compared to the observed conformation in the crystal structures (Table S1). For inhibitor **4b**, the ΔE values for the conformations when bound to CA II and the CA IX mimic were $0.282 \text{ kcalmol}^{-1}$ and $0.059 \text{ kcalmol}^{-1}$, respectively. The lower energy value for **4b** bound in the CA IX mimic indicates that the conformation of the inhibitor is close to its lowest energy conformation. These trends in energetic penalties match those of the dihedral angles measured

along carbon atoms C3-C4-C1'-C2', such that the more planar the conformations of each inhibitor resulted in a lower energy due to less unfavorable torsion angles. For inhibitor **4e**, the ΔE values for the conformations were 1.622 kcalmol⁻¹ and 0.373 kcalmol⁻¹, respectively. The energetic penalty for the inhibitor bound to CA II was higher most likely due to the strained dihedral angle between the linker and 4-aryl tail. For inhibitor **4p**, the ΔE values for the conformations when bound to the active sites of CA II and CA IX mimic were 1.256 kcalmol⁻¹ and 0.053 kcal mol⁻¹, respectively. Here again, the energetic penalty for the inhibitor bound to CA II is most likely due to the unfavorable dihedral angle between the linker ring and the 4-(3-quinoliny) tail. Although the angle is less strained than that observed for inhibitor **4e** in CA II, the added bulkiness of the tail in **4p** likely reduced the favorability of the conformation compared to the lowest-energy state. Although the trends in energy calculations aligned with the measured C3-C4-C1'-C2' dihedral angles of the inhibitors, they did not correlate with the K_i values (Table 2). This implies that the dihedral angle minimally contributed to the overall binding in the CA active site. The in vitro stopped-flow K_i measurements were instead a reflection of other factors, including active-site accessibility, solvent displacement, steric hindrance of residues within the active sites, and stability provided by vdW contacts and hydrogen bonds. These factors were not considered when calculating the in silico energetic penalty of the inhibitors in their various conformations, as these values solely consider the torsional constraints of the compound in a theoretical solution of water surrounded by an implicit water dielectric. Furthermore, the theoretical energy penalties calculated are relatively small, indicating that the small unfavorable torsion angles adopted by the inhibitors do not limit binding in the active site. Instead, the favorability of residue interactions and the exclusion of active-site water molecules are factors that play key roles in obtaining high affinity. Although these interactions sometimes result in unfavorable torsion angles, these energetic barriers

are easily overcome by the energetic gain of the interactions listed above. These results validate the importance of full characterization of the active sites of these drug targets in order to understand binding modes for higher ligand affinity and selectivity.

***In-silico* modeling of inhibitors in CA XII**

Inhibitors **4a**, **4b**, **4e**, and **4p** were also manually modeled into the active site of CA XII by using PDB ID: 1JCZ, with the ligand coordinates and geometric constraints from *Coot*[31] and *PHENIX*. [32] Compounds **4a** and **4b** fitted into the active site with ease with the 2-methyl group on **4b** pointing directly into the narrow hydrophobic pocket of the CA XII active site. Inhibitor **4e** was positioned with an additional hydrogen bond between the 3-formyl group and Ser135, a residue that differs between CA XII and CA I, II, and IX. This potential isoform-specific interaction and the overall larger hydrophilic region could be useful for exploiting specificity with CA XII. Alternatively, inhibitor **4p** (a more hydrophobic compound) could only be docked in an energetically unfavorable conformation, wedged along the narrow hydrophobic pocket of CA XII, with additional steric clashes with Ser132, especially due to the larger size of tail moiety of this inhibitor (Figure 3). The lack of favorable interactions are therefore likely reasons for the observed lower affinity for inhibitor **4p** with CA XII. Overall, smaller hydrophobic groups and larger polar groups will likely need to be used when binding to this isoform.

***In-silico* modeling of inhibitors in CA I**

Inhibitors were modeled into the active site of CA I by using PDB ID: 1HCB with the bicarbonate ion removed. Compounds **4a** and **4p** were modeled based on the high affinity measured in a stopped-flow kinetics assay for CA I of 42 and 35 nM, respectively. The active site of CA I is more

occluded than that of the other CA isoforms due to the positioning of Leu198 and His200 blocking the active site (Figure 4). Nevertheless, it is possible that these residues might alter their conformations upon ligand binding by twisting away. For a more insightful understanding of the binding modes of these inhibitors, crystal structures would be needed.

Conclusions

Differences in active-site residues between the CA isoforms play key roles in controlling affinity and accessibility of the studied inhibitors. Namely, residues at positions 65, 67, 69, 91, 131, 135, 170, and 204 (CA II numbering) differ between all or some of the isoforms studied. CA I contains bulkier ring side chains at His67, Phe91, and Tyr204, which limits accessibility of the four inhibitors. As such, the benzenesulfonamide inhibitors presented here are weaker (mm) CA I inhibitors. CA II contains Ala65, compared to Ser65 in other isoforms, resulting in the loss of a polar group in the hydrophilic region. In the hydrophobic region of CA II, Phe131 extends its bulky side chain farther into the active site compared to shorter Leu, Val, and Ala residues in CA I, IX, and XII, respectively, resulting in potential steric hindrance with bulky hydrophobic inhibitors. In CA IX, the hydrophobic pocket is comprised of only short, non-aromatic side chains, allowing the inhibitors to make several vdW interactions. CA IX also has Glu170 located in the hydrophilic region, compared to Lys170 in the other three isoforms, which could be a promising site for specific polar interactions for future designed CA IX-specific inhibitors. In CA XII, Lys67 extends farther into the active site than the shorter His, Asn, and Gln in the other isoforms (CA I, II, IX, respectively). CA XII active site also contains more hydrophilic groups such as Ser135 and Asn204, which result in a much larger hydrophilic region compared to the other isoforms. The overall geometry of the active sites reflects these residue differences, such that CA I is the least

accessible, followed by CA II, and CA XII and CA IX having the most solvent-exposed active sites.

The four inhibitors presented here in complex with various CA isoforms provide insight into specific interactions that contribute to selective inhibition. Although they all possess identical zinc binding groups and linker rings, variations in the 4-aryl tail have large effects on the measured binding affinities, leading to different binding interactions within each unique CA active site. In particular, compounds **4a**, **4b**, and **4p** had high affinity for CA IX, most likely due to the presence of more vdW contacts along the hydrophobic side of the active site, whereas compound **4e** was unable to form many specific interactions, due to the presence of the unfavorable 3-formyl group on the 4-aryl tail. Conversely, compound **4e** bound tightly to CA II, due to the formation of a hydrogen bond between the 3-formyl group and the side chain of Gln92. Compound **4e** was also modeled into CA XII and predicted to bind strongly, due to a potential hydrogen bond forming between the 3-formyl group and the side chain of Ser135, a residue that is specific to this CA isoform. Alternatively, compound **4p** bound weakly to CA XII, most likely due to the bulkiness of the hydrophobic 4-aryl tail that was unable to fit in the narrow hydrophobic region of this isoform's active site. All four inhibitors were able to make vdW contacts with the CA II active site, but the bulky Phe131 provided steric hindrance and caused the 4-aryl tail substituents to twist away from the face of the hydrophobic pocket. This reduced the amount of hydrophobic contacts that were possible compared to those that were present in the CA IX mimic, which had a smaller hydrophobic valine residue at position 131. The bulkiness of Phe131 in CA II also limited interactions between the inhibitors and Ile91, but these same inhibitors were able to bind more tightly in the CA IX mimic active site to interact with Leu91. These two residues at positions 91 and 131 seem to be key differences that might lead to isoform specificity between CA II and CA

IX.[33]

For the design of inhibitors against the cancer-associated CA IX, further modification of these inhibitors should be performed to exploit hydrophobic interactions along the CA IX active site that are inaccessible to CA II, with the primary focus on Phe131. In addition, the substitution of K170E between CA II and CA IX should be utilized by adding a long hydrophilic moiety extended from the existing 4-aryl tail. This addition can extend to the surface of the CA IX active site and form potential hydrogen bonds with Glu170 that would not be possible with Lys170 in CA II. Due to the wider active site of CA IX compared to CA II, these inhibitors targeting CA IX would require a correspondingly bulkier tail region to facilitate solvent displacement and limit accessibility into the CA II active site.

Although several inhibitors adopted twisted conformations by rotating along the linker-to-tail bond (C3-C4-C1'-C2') in the crystal structures, the calculated energetic penalty was minor in comparison to the highly favorable inhibition constants. This indicates that torsional constraints play a minor role in the energetic barrier of ligand binding, and the major energetic factors are controlled by ease of ligand entry and exit from the active site and the interactions the ligand makes with residues in form of vdW contacts and hydrogen bonds. It is therefore important to focus the study of isoform-based drug design on the modification of inhibitors to maximize isoform-specific interactions, regardless of the conformation strain it might place on the inhibitor. These insights advance our understanding of CA–ligand complexes in the design of high affinity, highly selective inhibitors towards continued exploration of treatments for various CA-related diseases, including aggressive forms of cancer.

Experimental Section

CA inhibition assay: CA-catalyzed CO₂ hydration activity methods were published previously by Cornelio et al.[29] as part of a larger series of benzenesulfonamide-based inhibitors with aryl substitutions in the para position of the benzene ring.

CA expression and purification: An engineered CA IX mimic was used for this study. The mimic is a chimeric protein of CA II containing seven active-site-residue mutations to resemble CA IX, allowing for ease of protein expression and crystallization.[34] The active-site mutations (A65S, N67Q, E69T, I91L, F131V, K170E, L204A) resulted in approximately 90% sequence homology between the mimic and wild-type CA IX active sites, such that drugs bound to the CA IXb mimic are representative of the interactions that would occur with the wild type enzyme.[34] Both the CA IX mimic and CA II were expressed in BL21(DE3) competent cells by growing plasmid-containing *Escherichia coli* cells in lysogeny broth supplemented with ampicillin (100 µg mL⁻¹). Upon reaching an OD₆₀₀ of 0.6, cultures were induced with isopropyl β-D-1-thiogalactopyranoside (IPTG), and protein was expressed for 4 h at 37°C with zinc sulfate (1M). Cells were mechanically and chemically lysed at 48°C, and protein was purified on a p-aminomethylbenzenesulfonamide agarose affinity column. Purity was assessed by SDS-PAGE and staining with Coomassie Brilliant Blue, with a known molecular weight of 30 kDa, and concentration was determined by UV/Vis spectroscopy at 280 nm with a molar extinction coefficient of 54800 cm⁻¹mol⁻¹. Each sample was concentrated by using Amicon Centricon molecular weight cutoff 10 kDa filters to achieve a final concentration of 20 mg mL⁻¹ of CA II and 41 mg mL⁻¹ of the CA IX mimic.

CA crystallization and inhibitor soaking: Crystallization conditions were prepared by using the Rigaku Alchemist in a 96-deep well plate to create a fine screen around the ideal CA II/IX mimic crystallization conditions of sodium citrate (1.6M), Tris·HCl (50 mM, pH 7.8). A final plate screened from sodium citrate (1.2–1.8M) and pH 7.2–8.8. CA II and CA IX mimic crystallization trays was prepared with the Gryphon Robot (Art Robbins Instruments) by using the sitting-drop vapor-diffusion method in a 96-well IntelliPlate. The CA II and CA IX mimic samples added to the plate were at a concentration of 20 and 40 mgmL⁻¹, respectively. Each large well contained 59.2 μ L of precipitant solution. Drops contained either 0.5 μ L of precipitant and 0.3 μ L of protein (top drop) or 0.3 μ L of precipitant and 0.3 μ L of protein (bottom drop) to create a final precipitant/protein ratio of 5:3 or 1:1, respectively. Crystal trays were sealed to allow for vapor diffusion to occur between the protein drop and precipitant well, and trays were stored at 25°C without agitation. Crystals were observed in multiple wells after one week. Following crystal formation, crystals were soaked with desired ligand for 24h prior to data collection. Stock solutions of each ligand were initially prepared by using 100% dimethyl sulfoxide (DMSO) and diluted to achieve a concentration of 1–5 mM (depending on solubility) of each ligand in a solution of 50% DMSO/water. These ligand solutions were further diluted into the well solution of each crystal at a ratio of 1:5 (ligand solution: well solution), and then 1–2 μ L were added to the crystal drop. Final concentrations of ligand added to crystal drops were at least 100 times higher than the reported K_i values. After 24 h incubation of ligand with the CA crystal, crystals were rapidly dipped in a solution of 20% glycerol (with precipitant solution and ligand) and mounted for X-ray data collection.

X-ray data collection: X-ray diffraction data was collected both inhouse and at the Cornell High Energy Synchrotron Source (CHESS). Data collected in house used a Rigaku RU-H3R rotating Cu anode generator with a wavelength of 1.5418 Å operating at 50 kV and 22 mA, fitted with Osmic mirrors and an R-Axis IV⁺⁺ image plate detector. Crystals were kept at 100 K during collection by cryogenic cooling with an Oxford CryoStream cooling system. Collection was performed by using the CrystalClear data collection package. The crystal to detector distance was set to 100 mm, with an oscillation angle of 1° and an exposure time of 7 min per image for 360 images. Data collected with this setup were **4a:** CA II, **4b:** CA II, **4e:** CA II, **4p:**CA II, **4p:**CA IX mimic. Data collected from CHESS data was completed on beamline F1 by using a 24-pole wiggler with an X-ray energy of 12.68 keV (0.98 Å). Data for the **4b:**CA IX mimic and **4e:**CA IX mimic were collected by using an ADSC Quantum 270 charge-coupled device (CCD) detector at a crystal-to-detector distance of 150 mm with a 1° oscillation angle and an exposure time of 2 s per image for 180 images. Data for **4a:** CA IX mimic were collected by using a Dectris Pilatus 6M CCD detector with a crystal-to-detector distance of 192 mm, ab 1° oscillation angle and an exposure time of 2 s per image for 180 images. All crystals were kept at 100 K during data collection by cryogenic cooling with an Oxford CryoStream cooling system. Collection was performed remotely by using an ALS-style BAM-1 crystal automounter and ADX data collection GUI.

X-ray data processing and refinement: All data were indexed, integrated, and scaled by using HKL2000[35] to a monoclinic $P2_1$ space group. The data were scaled to a resolution with the highest-resolution shell data showing completeness higher than 85% and linear R factors lower than 66 %. Molecular replacement (MR) was performed by using PHENIX Phaser-MR One-

Component Interface[32] with PDB ID: 3KS3 without zinc and solvent as the search model. For the refinement of structures containing CA IX mimic, the 3KS3 file used was modified to convert the CA IX mimic residues to alanine prior to MR. Refinement was performed by using *PHENIX* phenix.refine[32] and visualized by using Coot.[31] Prior to the first round of refinement, Rfree values were generated by setting aside 5% of the unique measured reflections, The necessary active-site mutations for CA IX mimic and the zinc atom were added, and this file was refined against the coordinates. Subsequent refinements were performed for refinement of the main-chain and sidechain residues, and the addition of solvent molecules. The ligand was added by using *Coot* LigandBuilder and *PHENIX* Ligands REEL to develop geometric restraints.[31, 32] The ligand PDB and geometric restraints were added to the overall structure and, after a final adjustment of all molecules (solvent, side chains, alternate conformations, ligand positions) was completed, a final round of refinement was performed. Analysis of interactions and bond angles were measured by using *Coot*. [31] The final F_o-F_c density is depicted in Figure S2.

Inhibitor free energy calculations: Geometry optimizations were performed at the M062X-D3/6-31G(d) level by using the Gaussian 09 program,[36] in which D3 indicates that Grimme's empirical dispersion correction[37] was added to the M062X functional. Solvent effects were considered by using the SMD implicit solvation model designed by Truhlar and co-workers.[38] Hydrogens were added to the inhibitors coordinates. Initially these structures were optimized by keeping the torsion dihedral angles fixed. This is a necessary step because the trial positioning for the hydrogens and experimental errors (from the crystal structures) on the positioning of the atoms could lead to significant energy differences. The structures were subsequently resubmitted to a complete geometry optimization (i.e., relaxing all degrees of freedom). The energy difference

between these two optimized conformations composes the reported values for ΔE in Table S1.

PDB IDs: 5SZ0, 5SZ1, 5SZ2, 5SZ3, 5SZ4, 5SZ5, 5SZ6, and 5SZ7. The authors will release the atomic coordinates and experimental data upon article publication.

Acknowledgements

The authors would like to thank the University of Florida Center for Structural Biology for the use of the in-house X-ray machine, and the Cornell High-Energy Synchrotron Source for use of their F-1 beamline and support from the beamline scientists and facility operators. Benedetta Cornelio is grateful for financial support from the Italian Ministry of Education, University, and Research (MIUR, PRIN 2010–2011—prot. 2010N3T9M4), Italian–French University (Vinci 2011), University of Chieti–Pescara, “Centre National de la Recherche Scientifique (CNRS)” and the University of Reims. G.A.R. and A.N.K. are grateful to the European Research Council (ERC) for financial support.

Conflict of Interest

The authors declare no conflicts of interest.

References

- [1] S. C. Frost in *Carbonic Anhydrase Mechanism, Regulation, Links to Disease, and Industrial Applications* (Eds.: S. C. Frost, R. McKenna), Springer, Utrecht, **2014**, pp. 9–30.
- [2] C. T. Supuran, *Nat. Rev. Drug Discovery* **2008**, *7*, 168–181.
- [3] B. P. Mahon, M. A. Pinard, R. McKenna, *Molecules* **2015**, *20*, 2323–2348.
- [4] J. E. Moulder, S. Rockwell, *Cancer Metastasis Rev.* **1987**, *5*, 313–341.
- [5] M. Hçckel, P. Vaupel, *J. Natl. Cancer Inst.* **2001**, *93*, 266–276.
- [6] D. Neri, C. T. Supuran, *Nat. Rev. Drug Discovery* **2011**, *10*, 767–777.
- [7] B. S. Peskin, M. J. Carter, *Med. Hypotheses* **2008**, *70*, 298–304.
- [8] N. Sadri, P. J. Zhang, *Cancers* **2013**, *5*, 320–333.
- [9] F. Cianchi, M. C. Vinci, C. T. Supuran, B. Peruzzi, P. De Giuli, G. Fasolis, G. Perigli, S. Pastorekova, L. Papucci, A. Pini, E. Masini, L. Puccetti, *J. Pharmacol. Exp. Ther.* **2010**, *334*, 710–719.
- [10] A. Innocenti, D. Vullo, J. Pastorek, A. Scozzafava, S. Pastorekova, I. Nishimori, C. T. Supuran, *Bioorg. Med. Chem. Lett.* **2007**, *17*, 1532–1537.
- [11] D. A. Whittington, A. Waheed, B. Ulmasov, G. N. Shah, J. H. Grubb, W. S. Sly, D. W. Christianson, *Proc. Natl. Acad. Sci. USA* **2001**, *98*, 9545–9550.
- [12] M. Benej, S. Pastorekova, J. Pastorek in *Carbonic Anhydrase Mechanism, Regulation, Links to Disease, and Industrial Applications* (Eds.: S. C. Frost, R. McKenna), Springer Netherlands, **2014**, pp. 199–219.
- [13] P. C. McDonald, S. Dedhar in *Carbonic Anhydrase Mechanism, Regulation, Links to Disease, and Industrial Applications* (Eds.: S. C. Frost, R. McKenna), Springer Netherlands, **2014**, pp. 255–269.
- [14] M.-J. Hsieh, K.-S. Chen, H.-L. Chiou, Y.-S. Hsieh, *Eur. J. Cell Biol.* **2010**, *89*, 598–606.
- [15] M. Aggarwal, C. D. Boone, B. Kondeti, R. McKenna, *J. Enzyme Inhib. Med. Chem.* **2013**, *28*, 267–277.
- [16] C. K. Tu, D. N. Silverman, C. Forsman, B. H. Jonsson, S. Lindskog, *Biochemistry* **1989**, *28*, 7913–7918.
- [17] J. F. Domsic, W. Williams, S. Z. Fisher, C. Tu, M. Agbandje-McKenna, D. N. Silverman, R. McKenna, *Biochemistry* **2010**, *49*, 6394–6399.
- [18] S. Z. Fisher, A. Y. Kovalevsky, J. F. Domsic, M. Mustyakimov, R. McKenna, D. N. Silverman, P. A. Langan, *Biochemistry* **2010**, *49*, 415–421.
- [19] Z. Fisher, J. A. Hernandez Prada, C. Tu, D. Duda, C. Yoshioka, H. An, L. Govindasamy, D. N. Silverman, R. McKenna, *Biochemistry* **2005**, *44*, 1097–1105.
- [20] C. T. Supuran, A. Scozzafava, A. Casini, *Med. Res. Rev.* **2003**, *23*, 146–189.
- [21] M. Aggarwal, R. McKenna, *Expert Opin. Ther. Pat.* **2012**, *22*, 903–915.
- [22] R. McKenna, C. T. Supuran, *Subcell. Biochem.* **2014**, *75*, 291–323.
- [23] V. Alterio, A. Di Fiore, K. D’Ambrosio, C. T. Supuran, G. De Simone, *Chem. Rev.* **2012**, *112*, 4421–4468.
- [24] M. Bozdog, M. Ferraroni, E. Nuti, D. Vullo, A. Rossello, F. Carta, A. Scozzafava, C. T. Supuran, *Bioorg. Med. Chem.* **2014**, *22*, 334–340.
- [25] M. A. Pinard, B. Mahon, R. McKenna, *BioMed Res. Int.* **2015**, *2015*, 1–15.
- [26] R. Gaspari, C. Rechlin, A. Heine, G. Bottegoni, W. Rocchia, D. Schwarz, J. Bomke, H.-D. Gerber, G. Klebe, A. Cavalli, *J. Med. Chem.* **2016**, *59*, 4245–4256.
- [27] N. Pala, L. Micheletto, M. Sechi, M. Aggarwal, F. Carta, R. McKenna, C. T. Supuran, *ACS Med. Chem. Lett.* **2014**, *5*, 927–930.

- [28] C. T. Supuran, *Bioorg. Med. Chem. Lett.* **2010**, *20*, 3467–3474.
- [29] B. Cornelio, M. Laronze-Cochard, M. Ceruso, M. Ferraroni, G. A. Rance, F. Carta, A. N. Khlobystov, A. Fontana, C. T. Supuran, J. Sapi, *J. Med. Chem.* **2016**, *59*, 721–732.
- [30] M. A. Pinard, C. D. Boone, B. D. Rife, C. T. Supuran, R. McKenna, *Bioorg. Med. Chem.* **2013**, *21*, 7210–7215.
- [31] P. Emsley, K. Cowtan, *Acta Crystallogr. Sect. D Biol. Crystallogr.* **2004**, *60*, 2126–2132.
- [32] P. D. Adams, P. V. Afonine, G. Bunkjcz, V. B. Chen, N. Echols, J. J. Headd, L.-W. Hung, S. Jain, G. J. Kapral, R. W. Grosse Kunstleve, A. J. McCoy, N. W. Moriarty, R. D. Oeffner, R. J. Read, D. C. Richardson, J. S. Richardson, T. C. Terwilliger, P. H. Zwart, *Methods* (San Diego, CA, U.S.) **2011**, *55*, 94–106.
- [33] B. P. Mahon, C. L. Lomelino, J. Ladwig, G. M. Rankin, J. M. Driscoll, A. L. Salguero, M. A. Pinard, D. Vullo, C. T. Supuran, S.-A. Poulsen, R. McKenna, *J. Med. Chem.* **2015**, *58*, 6630–6638.
- [34] C. Genis, K. H. Sippel, N. Case, W. Cao, B. S. Avvaru, L. J. Tartaglia, L. Govindasamy, C. Tu, M. Agbandje-McKenna, D. N. Silverman, C. J. Rosser, R. McKenna, *Biochemistry* **2009**, *48*, 1322–1331.
- [35] Z. Otwinowski, W. Minor, *International Tables for Crystallography, Crystallography of Biological Macromolecules*, Wiley, **2012**.
- [36] Gaussian 0.9, Revision E.01, M. J. Frisch, G. W. Trucks, H. B. Schlegel, G. E. Scuseria, M. A. Robb, J. R. Cheeseman, G. Scalmani, V. Barone, B. Mennucci, G. A. Petersson, H. Nakatsuji, M. Caricato, X. Li, H. P. Hratchian, A. F. Izmaylov, J. Bloino, G. Zheng, J. L. Sonnenberg, M. Hada, M. Ehara, K. Toyota, R. Fukuda, J. Hasegawa, M. Ishida, T. Nakajima, Y. Honda, O. Kitao, H. Nakai, T. Vreven, J. A. Montgomery, Jr., J. E. Peralta, F. Ogliaro, M. Bearpark, J. J. Heyd, E. Brothers, K. N. Kudin, V. N. Staroverov, R. Kobayashi, J. Normand, K. Raghavachari, A. Rendell, J. C. Burant, S. S. Iyengar, J. Tomasi, M. Cossi, N. Rega, J. M. Millam, M. Klene, J. E. Knox, J. B. Cross, V. Bakken, C. Adamo, J. Jaramillo, R. Gomperts, R. E. Stratmann, O. Yazyev, A. J. Austin, R. Cammi, C. Pomelli, J. W. Ochterski, R. L. Martin, K. Morokuma, V. G. Zakrzewski, G. A. Voth, P. Salvador, J. J. Dannenberg, S. Dapprich, A. D. Daniels, .: Farkas, J. B. Foresman, J. V. Ortiz, J. Cioslowski, D. J. Fox, *Gaussian, Inc.*, Wallingford, CT, **2009**.
- [37] S. Grimme, J. Antony, S. Ehrlich, H. Krieg, *J. Chem. Phys.* **2010**, *132*, 154104.
- [38] A. V. Marenich, C. J. Cramer, D. G. Truhlar, *J. Phys. Chem. B* **2009**, *113*, 6378–6396.

Figure Legends

Figure 1. Electron density of inhibitors. Calculated $2F_o-F_c$ maps of inhibitors bound in CA II and CA IX mimic active sites. Zinc is represented as a gray sphere. The figure is contoured to the 1.0 σ level and was generated by using *PyMOL*.

Figure 2. Crystal structures of inhibitors bound in CA II (gray) and CA IX mimic (cyan) active sites. All interactions depicted by gray dotted lines represent distances between 2.5–3.5 Å. The zinc atom is depicted as a gray sphere, solvent molecules are depicted as red spheres, oxygen atoms are displayed in red, and nitrogen atoms are shown in blue. Note that Leu91 in (H) is depicted in two conformations, as was evident from the density. The figure was generated by using *PyMOL*.
Crystal structures of inhibitors bound in CA II (grey) and CA IX-mimic (cyan) active sites. All interactions depicted by grey dotted line. Zinc atom depicted as grey sphere, solvent molecules depicted as red spheres, oxygen atoms as red, and nitrogen atoms as blue. Figure made using *PyMOL*.

Figure 3. Modeled structures of inhibitors in complex with CA XII (gold), with hydrophobic (orange) and hydrophilic (purple) regions of the active site labeled. The zinc atom is depicted as a gray sphere, oxygen atoms are red, and nitrogen atoms are blue. A potential hydrogen bond was observed between the formyl group on **4e** and Ser135 (white bond), with possible steric hindrance between the tail group of **4p** and Ser132 (white curves). This figure was generated by using *PyMOL*.

Figure 4. Modeled structure of inhibitors in complex with CA I (green), with hydrophobic (orange) and hydrophilic (purple) regions of the active site labeled. The zinc atom is depicted as a gray sphere, oxygen atoms in red, and nitrogen atoms in blue. Potential steric hindrance was observed between inhibitors **4a** and **4p** with His200 and Leu198 (white curves). The figure was

generated by using PyMOL.

Supplemental Figure 1.

Inhibitor **4e** in complex with CA II in the active site (blue box) and surface pocket (orange box).

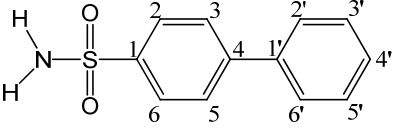
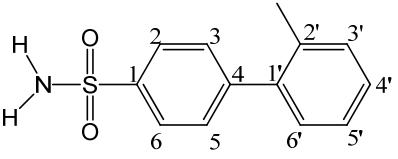
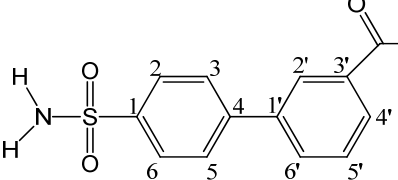
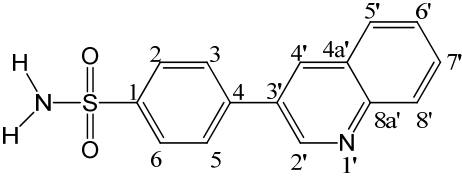
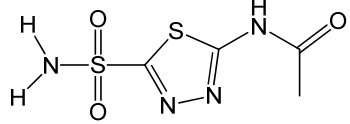
Glycerol molecule also shown complexed in active site (green). Figure made using *PyMOL*.

Table 1. Active site residue comparison

Residue Number	CA I	CA II	CA IX	CA XII
62	Val	Asn	Asn	Asn
64	His	His	His	His
65	Ser	Ala	Ser	Ser
67	His	Asn	Gln	Lys
69	Asn	Glu	Thr	Asn
91	Phe	Ile	Leu	Thr
92	Gln	Gln	Gln	Gln
121	Ala	Val	Val	Val
131	Leu	Phe	Val	Ala
135	Ala	Val	Leu	Ser
141	Leu	Leu	Leu	Leu
143	Val	Val	Val	Val
170	Lys	Lys	Glu	Lys
198	Leu	Leu	Leu	Leu
199	Thr	Thr	Thr	Thr
200	His	Thr	Thr	Thr
202	Pro	Pro	Pro	Pro
204	Tyr	Leu	Ala	Asn
207	Val	Val	Val	Val
209	Trp	Trp	Trp	Trp

Highlighted residues differ between isoforms with CA II numbering. V135L is unchanged in the CA IX mimic. Omitted: Tyr7, His94, His96, and His119, as they are conserved

Table 2. Compound inhibition profile

Compound	Nomenclature R- benzenesulfonamide	K_i (nM)			
		CA I	CA II	CA IX	CA XII
4a 	R= 4-(phenyl)	42	0.8	0.2	93
4b 	R= 4- (2-methylphenyl)	3500	1.2	20	47
4e 	R= 4- (3-formylphenyl)	1200	2.0	99	0.6
4p 	R= 4- (3-quinolinyl)	35	2.5	0.2	760
AZM 	acetazolamide	250	12	25	5.7

Inhibition profile of benzenesulfonamides with reference acetazolamide (non-isoform specific) for comparison. Compounds presented here are part of a larger series. K_i values are the average of $n=3$ runs with an experimental error of 5%..

Table 3. Compound fold selectivity for CA isoforms

Compound	Fold Selectivity				
	CA II/I	CA IX/I	CA IX/II	CA XII/I	CA XII/II
4a	50	200	4	<1	<<1
4b	3000	200	<1	80	<1
4e	600	10	<1	2000	3
4p	10	200	10	<1	<<1
AZM	20	10	<1	50	2

Calculated K_i ratios were from stopped-flow kinetics assay. A high selectivity for CA XII/I indicates preference for binding to CA XII over CA I, and low selectivity indicates preference for CA I binding.

Table 4. X-ray crystallography statistics for inhibitors bound to CA IX-mimic and CA II

Sample	CAIX-mimic: 4a	CA IX-mimic: 4b	CA IX-mimic: 4e	CA IX-mimic: 4p	CAII: 4a	CA II: 4b	CA II: 4e	CA II: 4p
PDB ID	5SZ0	5SZ1	5SZ2	5SZ3	5SZ4	5SZ5	5SZ6	5SZ7
Space Group	$P2_1$							
Cell Dimensions (Å;°)	$a = 42.2 \pm 0.2, b = 41.3 \pm 0.2, c = 72.5 \pm 0.4; \beta = 104.0 \pm 0.4$							
Resolution (Å)	20.0 – 1.60 (1.66 – 1.60)	20.0 - 1.28 (1.31 - 1.28) ^d	20.0 – 1.15 (1.18 – 1.15)	20.0 – 1.78 (1.84 – 1.78)	20.0 – 1.63 (1.67 – 1.63)	20.0 - 1.55 (1.60 – 1.55)	20.0 - 1.64 (1.67 – 1.64)	20.0 – 1.69 (1.76 - 1.69)
Theoretical Reflections	32093	63118	85976	45505	59321	35324	58969	27283
Unique Measured Reflections	27269	59116	84634	30697	48127	33540	49805	24873
R.M.S.D.: Bonds [Å]	0.008	0.010	0.008	0.006	0.006	0.007	0.006	0.006
Angles [°]	1.21	1.40	1.32	0.874	0.888	1.13	1.03	0.907
R_{pim}^a [%]	6.8 (66.8)	4.3 (26.3)	2.7 (21.4)	2.1 (12.0)	3.4 (25.7)	2.5 (33.0)	3.0 (19.2)	4.7 (27.1)
I/σ	10.7 (0.81)	29.0 (3.75)	44.4 (4.71)	35.9 (6.55)	18.7 (1.94)	27.3 (1.94)	26.2 (3.52)	12.0 (1.04)
Completeness [%]	97.8 (98.6)	94.4 (95.5)	98.8 (99.6)	98.7 (99.9)	96.3 (96.3)	95.8 (94.4)	94.2 (94.3)	98.2 (97.4)
R_{cryst}^b [%]	18.3 (23.9)	14.7 (20.1)	14.4 (21.6)	16.1 (19.4)	16.5 (29.8)	15.7 (27.1)	15.0 (22.8)	16.3 (28.8)
R_{free}^c [%]	21.7 (33.6)	16.5 (23.8)	15.9 (21.2)	19.5 (22.0)	19.2 (30.1)	18.5 (30.5)	18.0 (27.4)	20.3 (39.8)
Redundancy	3.2 (3.4)	3.3 (3.3)	6.3 (6.3)	3.4 (3.4)	5.0 (5.1)	3.8 (3.9)	5.4 (5.4)	6.5 (6.4)
# of Protein Atoms	2063	4071	4110	2057	2065	2078	2058	2070
Solvent	182	270	376	155	161	239	190	221
Ligand	28	32	30	33	28	32	60	33
Ramachandran stats [%]								
favored	97.2	97.2	96.4	96.1	97.2	96.9	96.5	97.2
allowe	2.77	2.77	3.56	3.95	2.77	3.15	3.53	2.77
outliers	0.000	0.00	0.00	0.00	0.00	0.00	0.00	0.00
Avg. B factors [Å ²]								

main-chain	15.9	15.7	13.7	15.0	16.0	11.1	12.0	18.6
side-chain	20.2	19.7	18.3	19.2	20.5	17.1	18.5	23.3
solvent	25.0	29.2	25.2	25.2	25.4	24.9	30.1	28.3
ligand	30.6 ^e	19.5	22.0	37.2	15.1	12.8	20.3	37.4

^a $R_{\text{pim}} = (\sum \sqrt{1/(n-1)} |I - \langle I \rangle| / \sum \langle I \rangle) \times 100$

^b $R_{\text{cryst}} = (\sum |F_o - F_c| / \sum |F_o|) \times 100$

^c R_{free} is calculated in the same way as R_{cryst} , but represents 5% of reflections omitted from refinement.

^d Values in parenthesis correspond to the highest resolution shell.

^e Ligand B factors calculated with occupancy = 1.

Figure 1. Electron Density of Inhibitors

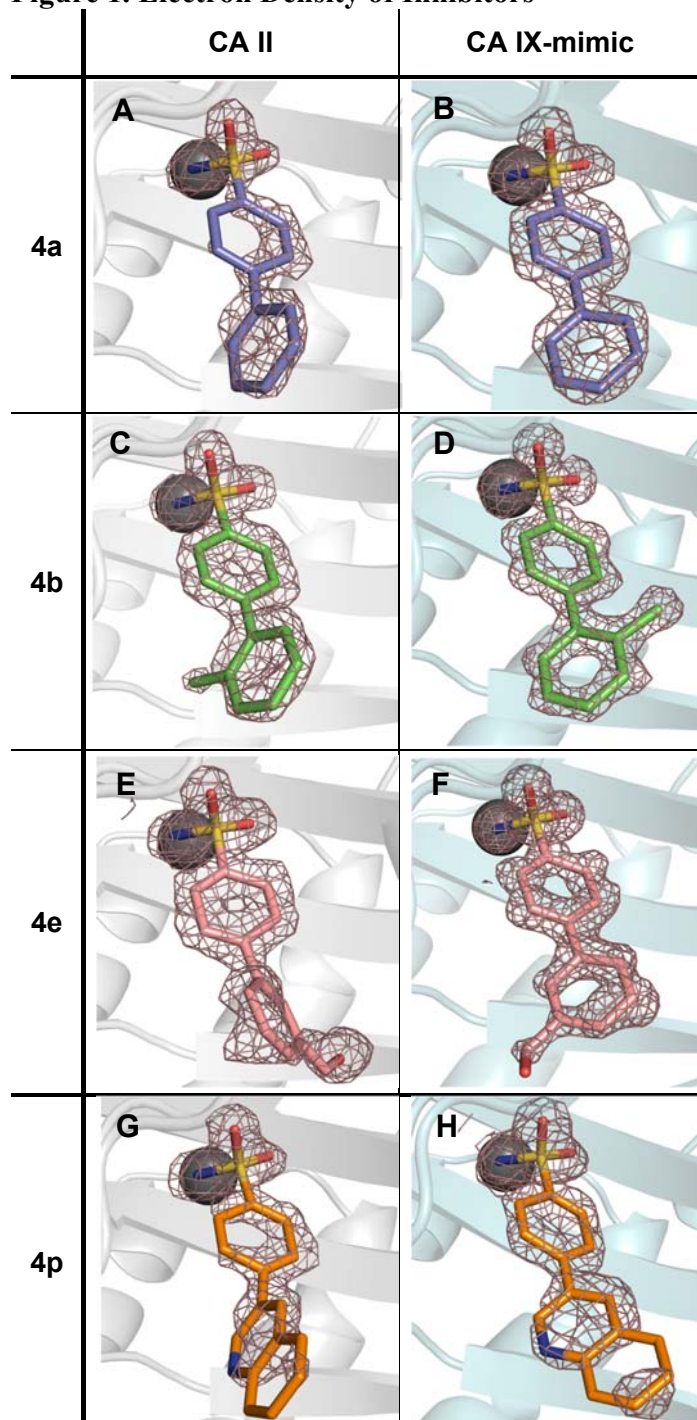
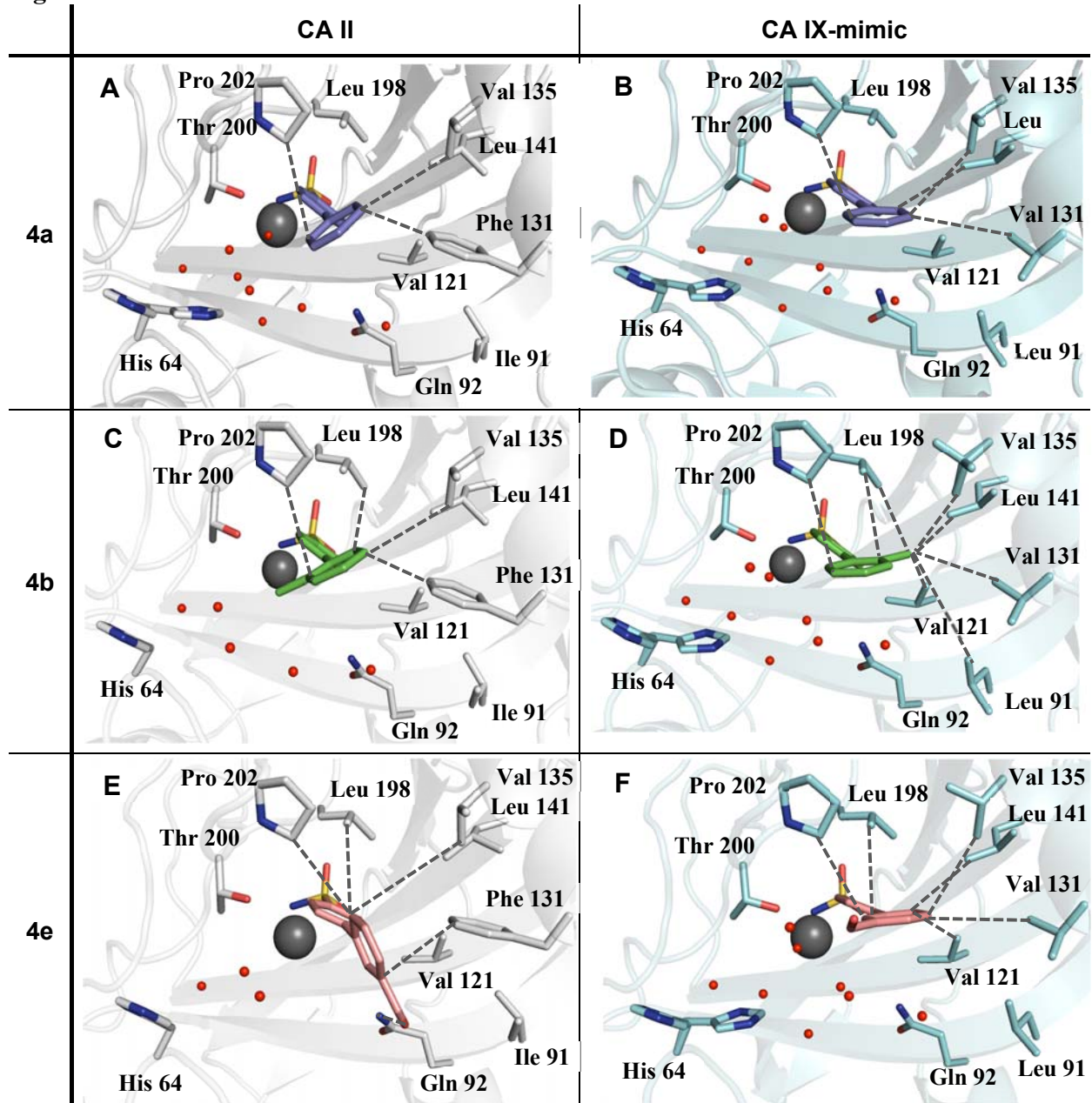


Figure 2. Inhibitor Interactions



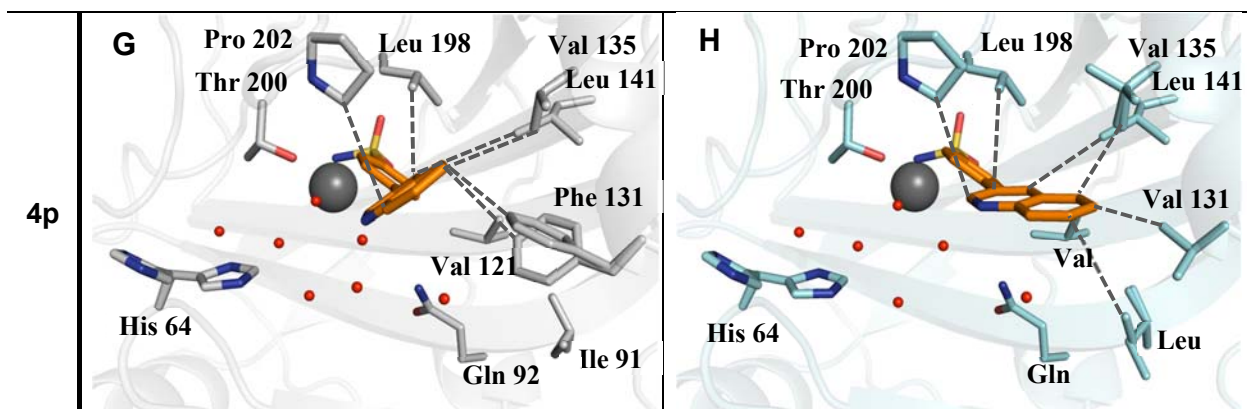


Figure 3. Docking of Inhibitors in CA XII

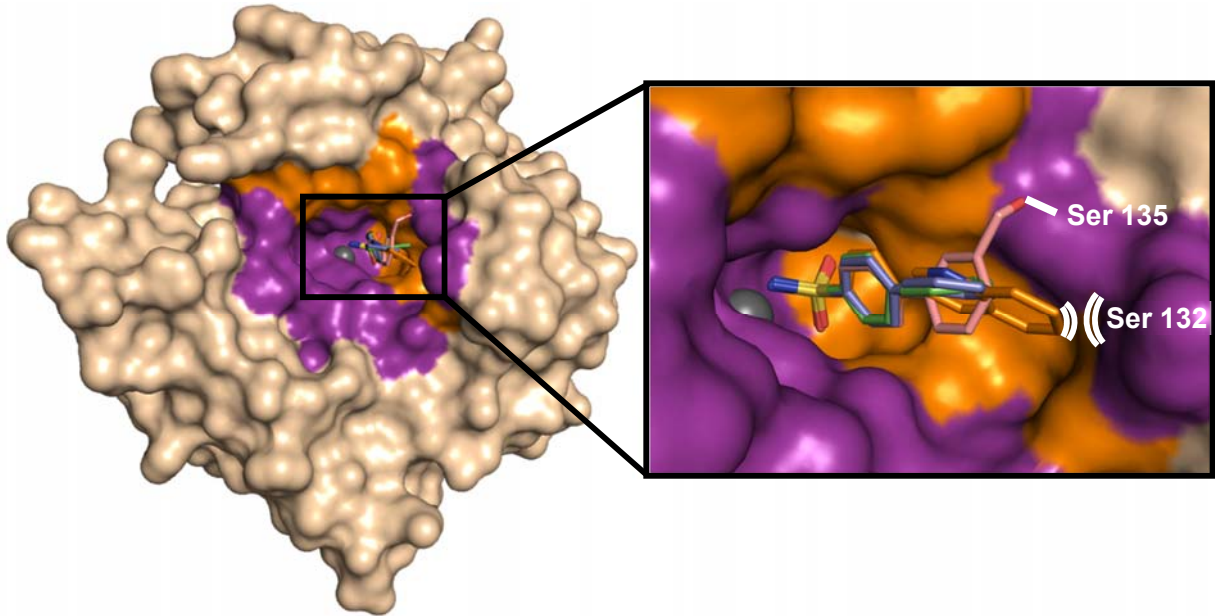
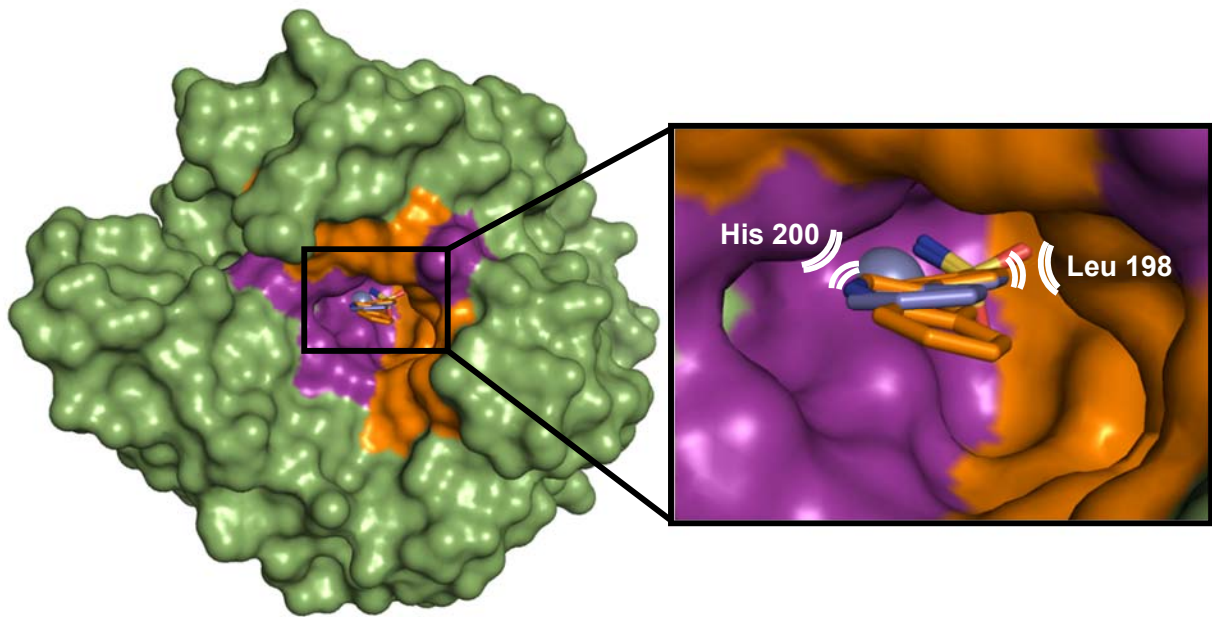
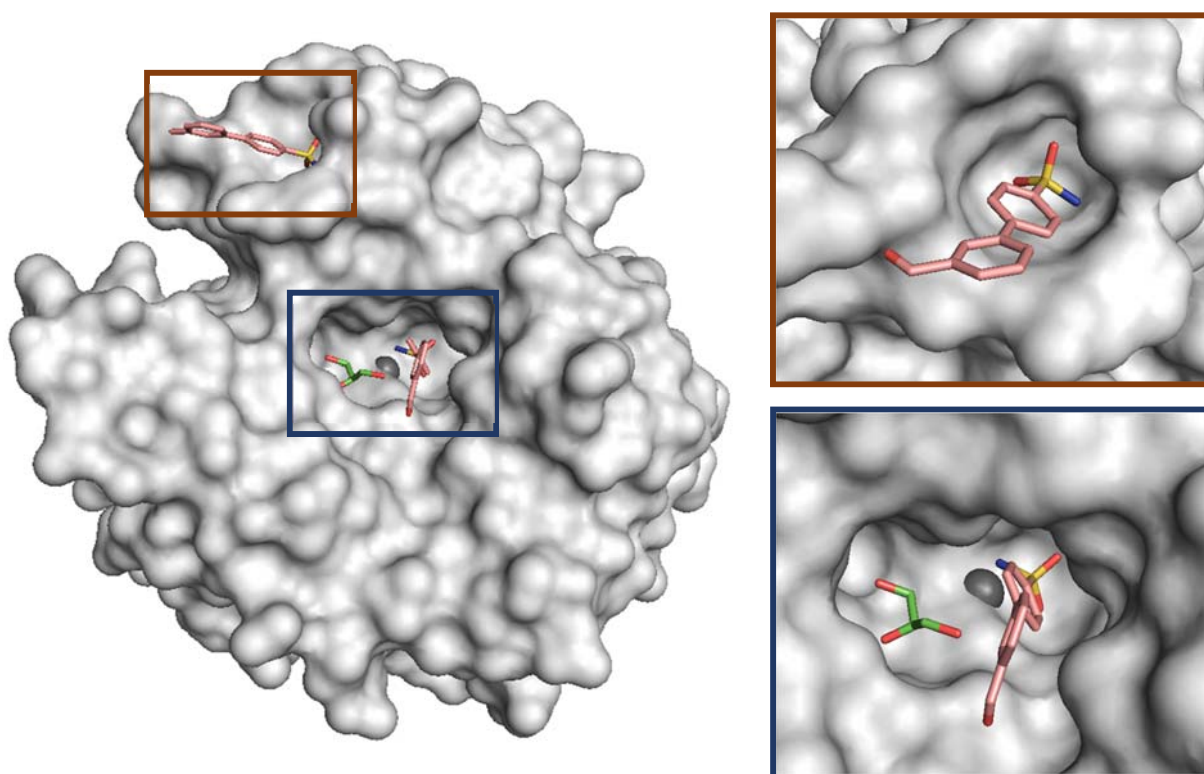


Figure 4. Docking of Inhibitors in CA I



Supplemental Figure 1. Compound 4e and glycerol molecule in complex with CA II



Supplemental Table 1. Inhibitor Free Energy Calculations

	CA II				CA IX-mimic		
	4b	4e (AS)	4e (CC)	4p	4b	4e	4p
ΔE (kcal/mol)	0.282	1.622	0.264	1.256	0.059	0.373	0.053

Calculation of energy associated with ligands in specific conformations observed in crystal structures. Values reflect the difference in energy (in kcal/mol) between the ideal geometry in solution compared to the conformation observed in crystal structure. Compound **4e** (AS) refers to the compound in the CA II active site and **4e** (CC) refers to the compound bound on the CA II surface.